ACS NANO
Cite This: ACS Nano 2018, 12, 12619−12628
www.acsnano.org

ARTICLE

Surface-Limited Superconducting Phase Transition on 1*T*-TaS_2

Ziying Wang,[†,#] Yi-Yang Sun,[‡,#] Ibrahim Abdelwahab,[†] Liang Cao,[§] Wei Yu,[†] Huanxin Ju,[⊥] Junfa Zhu,[⊥] Wei Fu,[†] Leiqiang Chu,[†] Hai Xu,[*,†,§] and Kian Ping Loh[*,†]

[†]Department of Chemistry, Centre for Advanced 2D Materials, National University of Singapore, Singapore 117543
[‡]State Key Laboratory of High Performance Ceramics and Superfine Microstructure, Shanghai Institute of Ceramics, Chinese Academy of Sciences, Shanghai 201899, China
[§]Changchun Institute of Optics, Fine Mechanics and Physics, Chinese Academy of Science, Changchun 130033, China
[⊥]National Synchrotron Radiation Laboratory, University of Science and Technology of China, Hefei 230026, China

S *Supporting Information*

ABSTRACT: **Controlling superconducting phase transition on a two-dimensional (2D) material is of great fundamental and technological interest from the viewpoint of making 2D resistance-free electronic circuits. Here, we demonstrate that a 1*T*-to-2*H* phase transition can be induced on the topmost monolayer of bulk (<100 nm thick) 1*T*-TaS_2 by thermal annealing. The monolayer 2*H*-TaS_2 on bulk 1*T*-TaS_2 exhibits a superconducting transition temperature (T_c) of 2.1 K, which is significantly enhanced compared to that of bulk 2*H*-TaS_2. Scanning tunneling microscopy measurements reveal a 3 × 3 charge density wave (CDW) in the phase-switched monolayer at 4.5 K. The enhanced T_c is explained by the suppressed 3 × 3 CDW and a charge-transfer doping from the 1*T* substrate. We further show that the monolayer 2*H*-TaS_2 could be switched back to 1*T* phase by applying a voltage pulse. The observed surface-limited superconducting phase transition offers a convenient way to prepare robust 2D superconductivity on bulk 1*T*-TaS_2 crystal, thereby bypassing the need to exfoliate monolayer samples.**

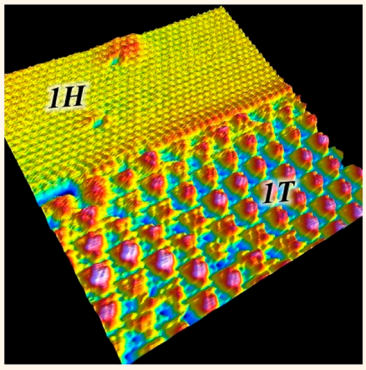

KEYWORDS: *2D materials, TaS_2, superconducting, surface phase transition, charge density wave*

Group-VB layered transition metal dichalcogenides (TMDs) MX_2 (M = Nb or Ta and X = S or Se) are ideal systems to explore various electronic ordering behaviors, including superconductivity and charge density waves (CDWs).[1,2] Different from group-IVB (Zr and Hf) and group-VIB (Mo and W) TMDs that are usually semiconductors with relatively large band gaps,[3−6] group-VB TMDs are metallic at room temperature and undergo superconducting phase transition at sufficiently low temperature. Another attractive aspect of group-VB TMDs is their vast varieties of atomic and electronic structures associated with the formation of CDWs,[2,7−9] therefore serving as good model systems for investigating the coexistence and competition between various charge-ordered states.[10−13] Polymorph transitions arising from different intralayer stacking in TaS_2 has been intensively researched with a view for controlling polymorph-specific properties such as metallic−insulator transition, superconductivity, and charge density wave order. In TaS_2, by a change of stacking order in response to pressure or temperature, the bulk crystal can adopt octahedral (1*T*), trigonal prismatic (2*H*), or other alternating configurations (4*Hb* and 6*R*).[2,14,15] 1*T*-TaS_2 has a rich phase diagram: metal above 543 K, incommensurate charge density wave (ICCDW) below 543 K, nearly commensurate charge density wave (NCCDW) below 350 K, and commensurate charge density wave ($\sqrt{13} \times \sqrt{13}$ CCDW) state below 200 K.[2,8,16,17] Bulk 1*T*-TaS_2 does not show superconductivity except when subjected to high pressure or intercalation of extrinsic elements.[12,18] In contrast, bulk 2*H*-TaS_2 develops 3 × 3 CDW modulation at 75 K and a superconductivity phase at 0.8 K.[2,19,20]

Metallic layered TMD compounds offer an opportunity to realize superconductivity down to monolayer thickness. From an application perspective, a monolayer superconductor presents the alluring prospect of a dissipationless device that can be miniaturized vertically and offer potential solutions to the thermal management issues facing current silicon-based complementary metal oxide semiconductor (CMOS) technology.[21] At the atomically thin limit, the competition between electron−phonon coupling, electron−electron interactions, and disorder provides stabilization or destabilization forces to

Received: September 27, 2018
Accepted: November 7, 2018
Published: November 7, 2018

DOI: 10.1021/acsnano.8b07379
ACS Nano 2018, 12, 12619−12628

the charge-ordered state. In particular, the microscopic formation mechanism of CDW and superconducting phases at the atomically thin limit is not well understood.[17,18] Recent work reported that vertically scaling the thickness of 2D materials can change the superconducting transition temperature (T_c). In 2*H*-$NbSe_2$, for example, T_c was found to decrease from the bulk value of 7.2 K to between 1 and 3 K for the monolayer,[10,11,22−24] and this has been attributed to the enhancement of electron−phonon coupling constants.[25] In contrast, enhanced T_c had been reported on few-layer 2*H*-TaS_2;[11,25,26] a T_c of 3.4 K is reported on monolayer 2*H*-TaS_2, as compared to 0.8 K of the bulk crystal. The suppression of CDW order, which competes with superconducting pairing, has been proposed to be responsible for the enhanced T_c in 2*H*-TaS_2.[25]

Phase-controlled synthesis of TMDs offer a strategy to fabricate metal/semiconductor or metal/superconductor transition for electronic applications.[27,28] It is technically challenging to prepare monolayer 2*H*-TaS_2 by chemical vapor deposition or mechanical exfoliation; thus a reliable and scalable method for preparing a superconducting monolayer is highly desirable. A monolayer superconductor is prone to electronic instability arising from interfacial electron−phonon coupling.[29,30] To reduce interfacial lattice strain experienced by a monolayer 2*H* flake on a heterosubstrate, one strategy is to create 2D superconductivity on the surface of a bulk crystal. For example, 2D superconductivity with an effective thickness of 1.5 nm has been induced on bulk MoS_2 flakes that are tens of nanometer in thickness by ionic gating.[31]

Herein, we investigate surface-limited polymorph conversion on a 1*T*-TaS_2 crystal that is tens of nanometer thick by exploiting the tendency for surfaces to undergo thermally induced relaxation, whereby the conversion of the surface to a monolayer 2*H* polymorph creates 2D superconductivity on a bulk crystal. The polymorph conversion has been verified by scanning tunneling microscopy (STM) to be restricted to the topmost layer. In addition, we performed transport measurements and found that the 2*H*-1*T* heterostructure device behaves as a metal without a Mott phase transition and exhibits a superconducting transition at 2.1 K, which is about 3 times higher than the T_c of bulk 2*H*-TaS_2. Our work demonstrates a simple approach to induce monolayer superconductivity on bulk crystal by allowing the surface to undergo polymorph transition, leading to an insulator−superconductor van der Waals (vdW) heterostructure.

RESULTS AND DISCUSSION

Figure 1 shows the relative stability of the 1*T* and 2*H* polymorphs for monolayer TMDs calculated using density functional theory (DFT). It is clear that the energy differences between the 1*T* and 2*H* polymorphs of group-VB TMDs are significantly smaller than those for group-IVB and group-VIB TMDs. In particular, TaS_2 possesses an energy difference of less than 0.1 eV per formula unit (f.u.) between the 1*T* and 2*H* polymorphs, which is possibly the smallest energy difference between the two polymorphs among known TMDs; thus it is chosen for this study due to the possibility of achieving facile polymorph conversion by heat or electrical energy.

Figure 2b shows the topography of an as-cleaved 1*T*-TaS_2 sample obtained using STM at 77.8 K. It is known that at this temperature, 1*T*-TaS_2 exists in the CCDW phase accompanied by a $\sqrt{13} \times \sqrt{13}$ reconstruction of the atomic lattice.[2,8,17,32] A

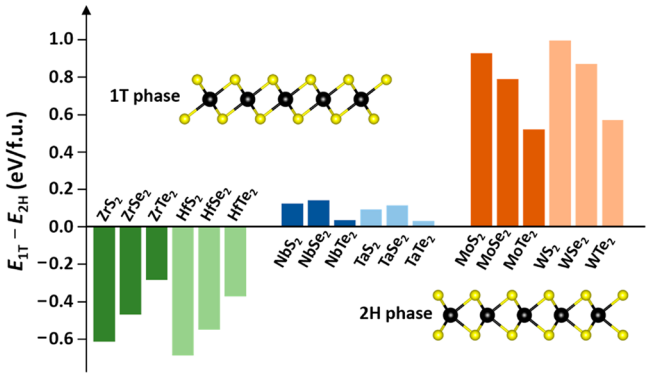

Figure 1. Energy difference between 1*T* and 2*H* polymorphs of group-IVB, VB, and VIB TMDs. Data were obtained using DFT calculation with the SCAN+rVV10 functional. While the most stable polymorphs for some of the tellurides, e.g., $NbTe_2$, $TaTe_2$, and WTe_2, are various distorted 1*T* polymorphs, we included these materials in the plot to illustrate the general trend.

zoom-in view in Figure 2c confirms the CCDW phase with a measured distance of about 12.1 Å between the centers of two bright spots. Figure 2d shows the differential conductance (d*I*/d*V*) spectrum on the CCDW surface (black line), which resolves two prominent peaks located at −0.24 eV (lower Hubbard band) and 0.19 eV (upper Hubbard band), respectively, thus opening a Mott gap of 0.43 eV. Beyond the lower Hubbard band, the peak at −0.35 eV is due to the top of subvalence band of TaS_2. A dip around −0.3 eV that splits the lower Hubbard peak and the valence peak is ascribed to the CDW formation. The shape of the d*I*/d*V* spectrum is consistent with previous reports of 1*T*-TaS_2.[8,17]

The sample was then subjected to thermal annealing at above 250 °C in ultrahigh vacuum (UHV). Figure 2e shows the surface topography after annealing. Under the same tunneling condition, i.e., bias, current and temperature, the surface topography exhibits a significant change from that before annealing (Figure 2b). A zoom-in view in Figure 2f shows that the surface periodicity changes to 1 × 1, which we attribute to a transition to 2*H* polymorph because a 1 × 1 periodicity is unexpected on the surface of the 1*T* polymorph at this temperature. The d*I*/d*V* spectrum recorded on this 1 × 1 surface, as shown in Figure 2d (red line), reveals a metallic state with a finite density of states (DOS) around the Fermi level (E_F). The two Hubbard peaks observed on the as-cleaved 1*T*-TaS_2 surface disappear. In addition, a sharp peak (marked by green arrow) at −0.35 eV appears, the origins of which are due to convoluted DOS from both 2*H* and 1*T* polymorphs, according to DFT calculations (Figure 6e). It indicates that the top surface has transferred to the 2*H* polymorph from the original 1*T*, as shown in Figure 2a. A small dip in the d*I*/d*V* spectrum with shoulders at −0.1 and 0.05 V is observed, arising from the indirect gap between Ta-dz^2 bands near Fermi surface and higher Ta-d bands.[33,34]

Devices were fabricated on samples before and after annealing to study the emergence of superconductivity. The resistance−temperature (*R*−*T*) curves were measured using a four-probe device configuration (Supplementary Figure S1) and displayed in Figures 3a and b. The 1*T*-TaS_2 sample without annealing shows a typical semiconducting behavior; that is, the resistance increases with the temperature decreasing. The sudden increase of resistivity at 185 K indicates a transition from the NCCDW to the CCDW

DOI: 10.1021/acsnano.8b07379
ACS Nano 2018, 12, 12619−12628

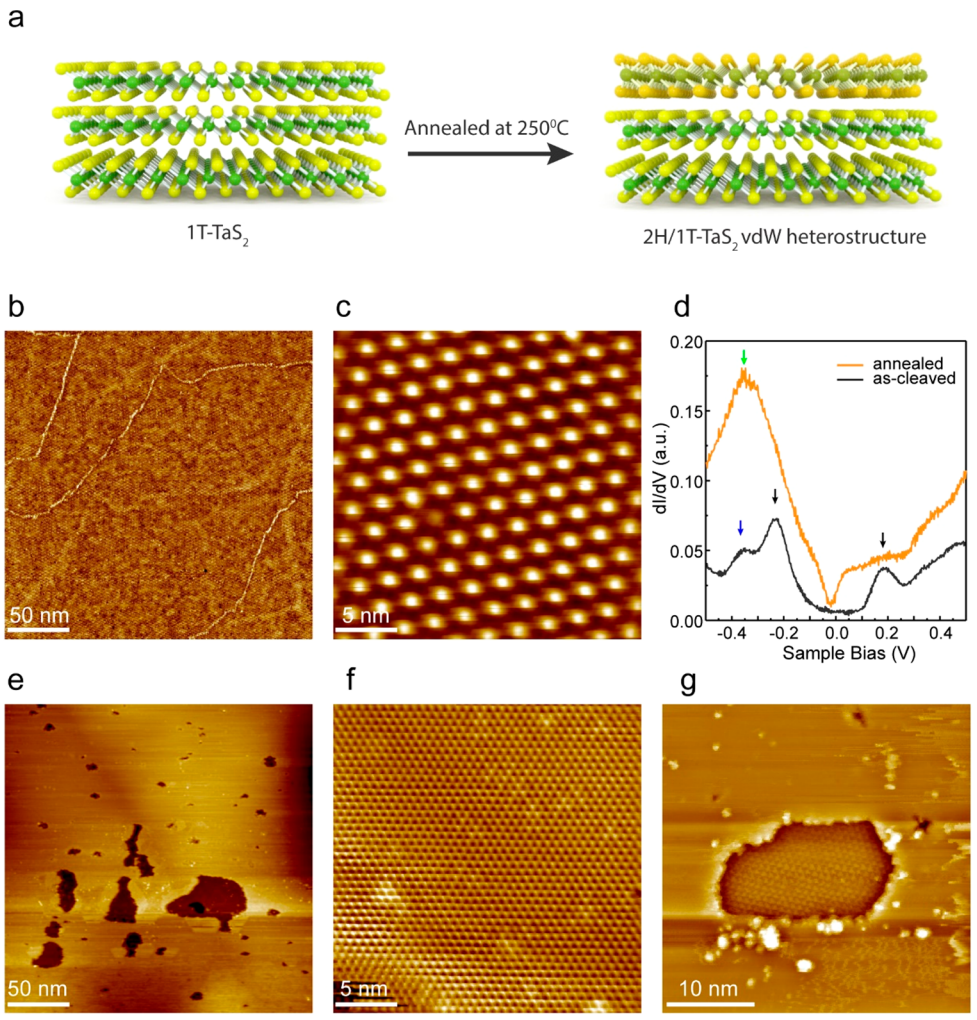

Figure 2. Polymorph transition on the 1*T*-TaS_2 surface by thermal annealing. (a) Schematic of a monolayer polymorph transition occurring in the topmost monolayer of 1*T*-TaS_2. (b) STM topography of the as-cleaved 1*T*-TaS_2 surface. Scale bar, 50 nm. (c) Zoom-in view of the as-cleaved 1*T*-TaS_2 surface showing the CCDW phase with a $\sqrt{13} \times \sqrt{13}$ periodicity. Scale bar, 5 nm. (d) d*I*/d*V* spectra recorded on the 1*T*-TaS_2 surface before (black) and after (red) thermal annealing. The arrow marks are discussed in the text. (e) STM topography of a 1*T*-TaS_2 surface after annealing at 250 °C. Scale bar, 50 nm. (f) Zoom-in view of the annealed surface showing a 1 × 1 periodicity. Scale bar, 5 nm. (g) Zoom-in view of a pit on the annealed surface showing $\sqrt{13} \times \sqrt{13}$ periodicity in the pit and 1 × 1 periodicity outside. Scale bar, 10 nm. All STM/STS data were obtained at 77.8 K.

phase.[2,7,35] Upon heating, the reverse transition from CCDW to NCCDW exhibits a hysteresis with a transition temperature of 260 K; essentially, the *R*−*T* curve is consistent with that of 1*T*-TaS_2, as reported previously.[2,12,20]

In sharp contrast, the annealed sample shows a metallic behavior; that is, the resistance decreases as temperature decreases. As shown in Figure 3b, the resistance varies linearly with temperature until T_c, which is attributed to phonon-limited resistivity and characteristic of metallic behavior. The inset of Figure 3b shows that the superconducting transition occurs at about 2.1 K. It is well known that 2*H*-TaS_2 presents a superconducting phase; therefore we attribute the presence of superconductivity to a 1*T*-to-2*H* surface polymorph transition. Since the 2*H* polymorph is far more conducting than the insulating 1*T* polymorph, especially at low temperature, the 2*H* phase dominates the electrical transport properties. It is important to note that the T_c observed here is about 3 times that of bulk 2*H*-TaS_2 and its *R*−*T* relation deviates from the trends reported for bulk or few-layer 2*H*-TaS_2 devices.[11,20,25] The residual resistance in the superconducting phase is nonzero; this is due to crystal imperfections in the fabricated 2*H*-TaS_2 monolayer.[26] It was reported previously that at 70 K the bulk 2*H* phase undergoes a quick drop in resistance, which is due to the appearance of 3 × 3 CDW; however such a fingerprint feature is absent in the *R*−*T* curve in Figure 3b, suggesting that the 3 × 3 CDW phase is suppressed to much lower temperatures.

To further characterize the electronic transport property of the 2*H*-1*T* heterostructure formed by the surface 1*T*-to-2*H* polymorph transition, an out-of-plane magnetic field was applied to the sample. Figure 3c shows the *R*−*T* curves at various perpendicular magnetic fields. T_c is gradually lowered as the field strength increases, which is a typical feature of a type-II superconductor.[36,37] Figure 3d shows longitudinal resistance as a function of perpendicular magnetic field at various temperatures. The magnetoresistance in the superconductivity range is positive. The 2*H*-1*T* heterostructure presents an upper critical field (B_{c2}) of 1.4 T at 250 mK. The 2D nature of this superconductivity can be deduced from the superconducting coherence length of monolayer 2*H*-TaS_2,

DOI: 10.1021/acsnano.8b07379
ACS Nano 2018, 12, 12619−12628

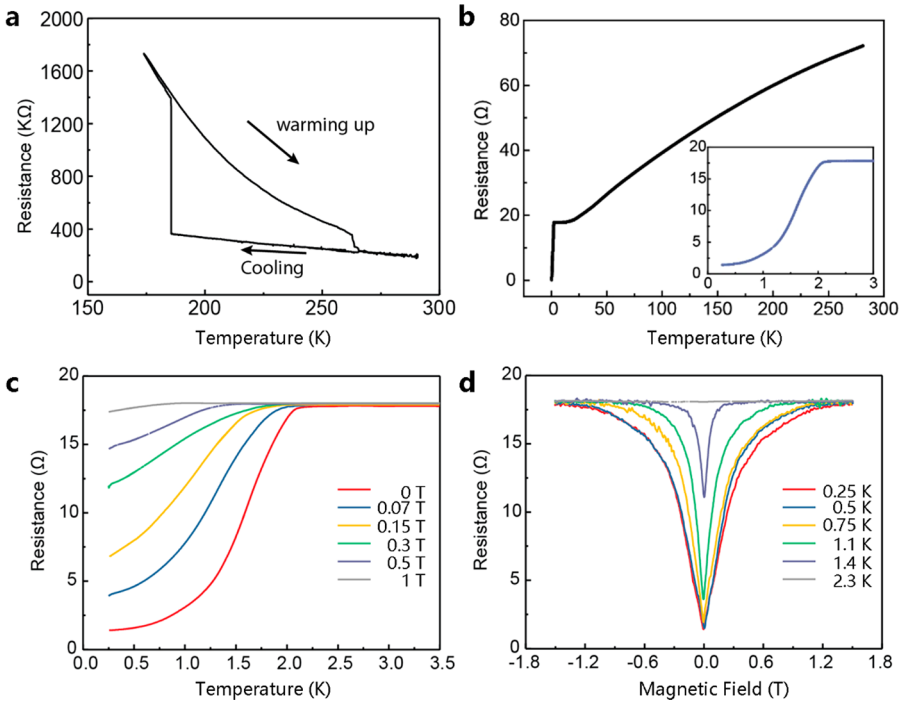

Figure 3. Electrical transport measurements of the 1*T*-TaS_2 samples without and with thermal annealing. (a) In-plane resistance as a function of temperature ($R-T$ curve) of the 1*T*-TaS_2 sample without annealing. The NCCDW-to-CCDW phase transition occurs at 185 K, and the CCDW-to-NCCDW phase transition occurs at 260 K. (b) $R-T$ curve recorded on the annealed 1*T*-TaS_2 sample showing a superconducting transition at 2.1 K, as highlighted in the inset. (c) $R-T$ curves of annealed 1*T*-TaS_2 in the superconducting range under varying magnetic fields perpendicular to the surface. (d) Resistance as a function of the perpendicular magnetic field of annealed 1*T*-TaS_2 at varying temperatures.

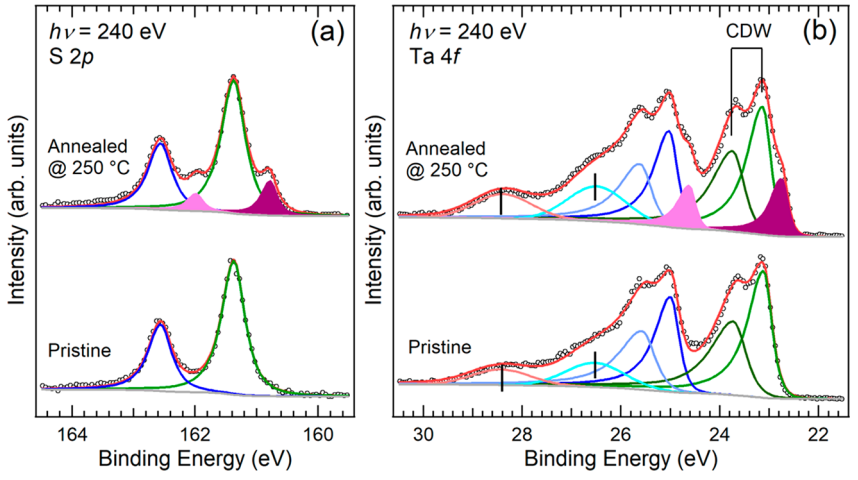

Figure 4. XPS spectra of the 1*T*-TaS_2 surface before and after annealing, showing the S 2p and Ta 4f core levels. As labeled in the plots, "pristine" indicates the sample before annealing, and "annealed@250 °C" indicates the plot of the sample after annealing.

which is calculated to be 15.3 nm according to the equation $B_{c2} = \frac{\varphi_0}{2\pi\xi^2}$, where $\varphi_0 \approx 2.07 \times 10^{-15}$ Wb and ξ is the superconducting Ginzburg–Landau (GL) coherence length.[38] This value is larger than the thickness of the monolayer 2*H*-TaS_2 and close to recent results reported on few-layer 2*H*-TaS_2 flakes,[26] suggesting that the superconductivity is in the 2D limit.

As bulk 1*T*-TaS_2 is not superconducting, the observed superconducting transition in Figure 3b should originate from the polymorph-converted monolayer 2*H*-TaS_2. STM imaging, which directly probes the top 1 or 2 layers of the sample surface, provides strong evidence that a monolayer 2*H*-TaS_2 is created on top of the bulk 1*T*-TaS_2. On the annealed surface, there are broken areas (or pits) where lower layers are exposed, thus allowing the first and second layer to be differentiated. The STM line profile across the edge of the pits reveals that the height of the edge is about 0.6 nm, which is equivalent to the thickness of a TaS_2 monolayer (Supplementary Figure S2). Atomic resolution STM images within the pits show that the bottom layer preserves the $\sqrt{13} \times \sqrt{13}$ CCDW phase, whereas the topmost layer shows a 1×1 phase (see Figure 2g as well as Supplementary Figure S2 obtained on another pit from the surface).

DOI: 10.1021/acsnano.8b07379
ACS Nano 2018, 12, 12619–12628

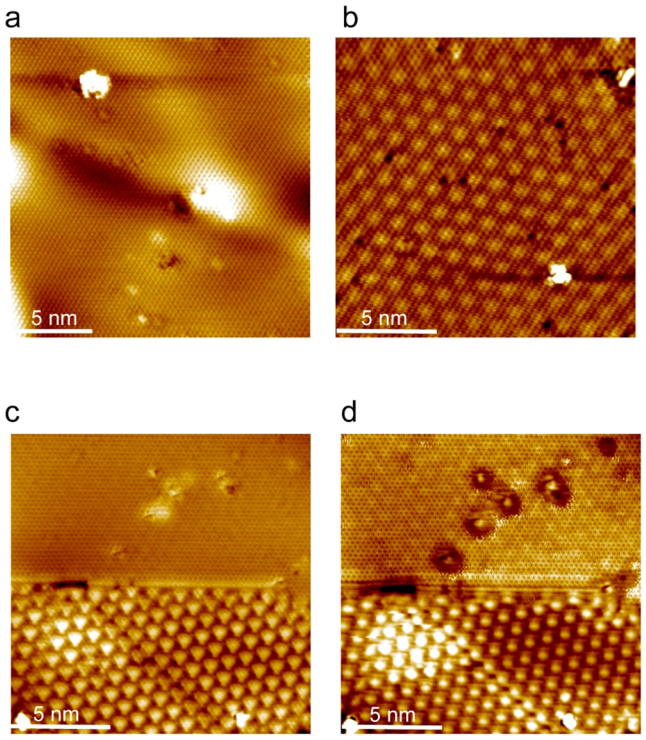

Figure 5. Polymorph transition excited by applying a tip voltage pulse in the annealed *1T*-TaS_2 surface. (a) STM image of the annealed 1*T*-TaS_2 surface with relatively low negative bias (V_g = −0.5 V, I_t = 300 pA), showing 1 × 1 periodicity. (b) Similar to (a), but with a relatively high positive bias (V_g = 1 V, I_t = 300 pA), where a $\sqrt{13} \times \sqrt{13}$ superstructure is superposed on the 1 × 1 lattice. (c) STM image of the annealed 1*T*-TaS_2 surface after applying a voltage pulse of V_g = 3 V for 300 ms. Imaging condition is V_g = −0.5 V and I_t = 300 pA. (d) Similar to (c), but with imaging condition V_g = 1 V and I_t = 300 pA. All images in this figure were obtained at 77.8 K. Scale bar is 5 nm in all images.

Our results indicate that thermal annealing provides the activation energy for transforming the 1*T* to the more stable 2*H* phase. Under our UHV annealing condition, the phase transition is limited to the surface, due possibly to the greater ease of structural relaxation of surface atoms. Raman spectroscopy was also used to track the polymorph transition (Supplementary Figure S4). The CCDW folded-back peaks[39] were observed before and after annealing, indicating that the deeper layers of the crystals retained their *1T* polymorph structure and were not degraded by heating, as shown in Figure S4. However, although we are able to see the 1*T*-to-2*H* polymorph transition using STM, we are not able to resolve the 2*H* phase clearly by Raman spectroscopy due to its surface-limited thickness and the overlap of the 2*H* signal with the 1*T* phase.[40,41]

In order to further confirm this 1*T*-to-2*H* polymorph transition after thermal annealing, high-resolution photoemission spectroscopy was conducted. As shown in Figure 4, the evolution of the S 2p and Ta 4f spectrum after annealing clearly shows that the 2*H* phase appears in the 1*T*-TaS_2 sample. The S 2p core-level spectrum of pristine 1*T*-TaS_2 shows well-resolved peaks at 161.4 ($2p_{3/2}$) and 162.6 eV ($2p_{1/2}$), which agrees well with the reported S 2p spectrum of 1*T*-TaS_2.[42] After annealing at 250 °C for 2 h in UHV, new peaks at 160.8 eV ($2p_{3/2}$, purple) and 162.0 eV ($2p_{1/2}$, pink) appear, which are the signature peaks of S 2p for the 2*H* phase TaS_2.[43] The Ta 4f core-level spectra of 1*T*-TaS_2 before and after annealing are shown in Figure 4b. The peaks located at 23.1, 25.0 eV, and 23.7, 25.6 eV are attributed to the CDW phase of 1*T*-TaS_2.[44] A new doublet component with binding energies of ∼22.8 and ∼24.7 eV (filled with purple and pink) is observed for the annealed sample, which is attributed to Ta^{4+} $4f_{7/2}$ and Ta^{4+} $4f_{5/2}$ of 2*H*-TaS_2.[42]

To rule out that the possibility that the surface phase change we observed is due to different sample thickness or substrate effects, we have prepared samples of different thickness and placed them on either Au/Si or SiO_2/Si substrates. The results show that the phase transition is independent of sample thickness and substrate and only dependent on the annealing temperature. We also did not observe a significant increase of defect density on the TaS_2 surface before and after annealing by using STM.

Another evidence for the phase change being limited only to the topmost layer is from bias-dependent STM images on the 1 × 1 region (*i.e.*, away from the pits). Using different tip bias voltages, we can see through the top layer so that the $\sqrt{13} \times \sqrt{13}$ CCDW phase in the second layer can be imaged simultaneously with the 1 × 1 phase of the topmost layer. As shown in Figure 5a and b, only a 1 × 1 surface structure is observed on the top 2*H* polymorph at a low negative bias using STM. At high positive tip bias, the 1 × 1 surface structure is overlapped by a $\sqrt{13} \times \sqrt{13}$ CDW arising from the underlying *1T* polymorph.

To switch off the superconducting state of the 2*H* monolayer, an external stimulus is necessary. Applying a voltage pulse by an STM tip had been found to induce the 2*H*-to-1*T* polymorph transition;[45] similarly, we observed that a bias voltage above +2.5 V can induce a 2*H*-to-1*T* polymorph transition. The effective area of the polymorph transition depends on the applied voltage. As shown in Figure 5c and d, after a voltage pulse, two distinct polymorphs, with unit cells of $\sqrt{13} \times \sqrt{13}$ and 1 × 1 periodicity, respectively, and separated by a domain boundary can be clearly resolved in the STM image. Our work hints at the possibility of inducing a global 2*H*-to-1*T* phase transition by driving an electrical current through the sample, which would be ideal for achieving controlled switching between the non-superconducting and superconducting phases.

To understand the energetics of the thermally induced phase transition, it is instructive to calculate the enthalpy of formation for monolayer TaS_2 in 1*T* and 2*H* polymorphs, with and without CDWs. The $\sqrt{13} \times \sqrt{13}$ CDW of the 1*T* polymorph is characterized by a Star-of-David-shaped atomic lattice,[32] as shown in Figure 6a. For the 2*H* polymorph, however, the 3 × 3 CDW is only observed at temperatures below 77 K.[25,46] Our DFT calculations reveal that free-standing monolayer 2*H*-TaS_2 with 1 × 1 structure is 88 meV/f.u. more stable than the 1*T* polymorph. Although the $\sqrt{13} \times \sqrt{13}$ CDW reconstruction, as shown in Figure 6a, significantly lowers the energy of the 1*T* polymorph by about 58 meV/f.u., its energy is still higher than the 2*H* polymorph. The 2*H* polymorph could be further stabilized by about 13 meV/f.u. through the formation of the 3 × 3 CDW. We considered various possible structures for the 3 × 3 CDW,[47] and the one with the lowest energy is shown in Figure 6a, where the longest and shortest Ta−Ta distances are 3.44 and 3.15 Å, respectively, compared to 3.32 Å in the case of the 1 × 1 structure. Taken together, our calculation suggests that the 2*H* polymorph is lower in energy than the 1*T* polymorph by about

DOI: 10.1021/acsnano.8b07379
ACS Nano 2018, 12, 12619−12628

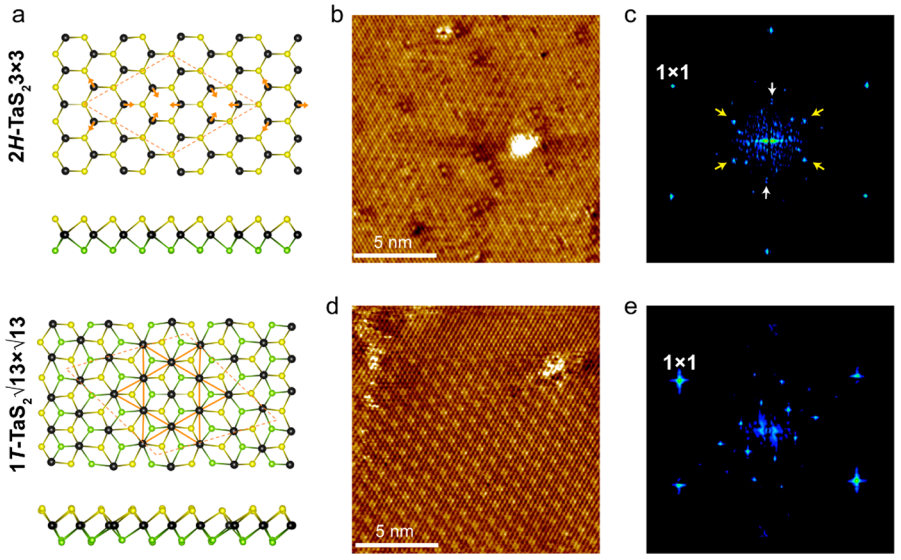

Figure 6. CDWs of the annealed 1*T*-TaS_2 surface at different temperatures. (a) Top and side views of atomic structures of the 3 × 3 2*H* polymorph and the $\sqrt{13} \times \sqrt{13}$ 1*T* polymorph. Arrows in the top view of the 3 × 3 2*H* polymorph show the directions of the atomic displacements. Brown-colored lines in the top view of the $\sqrt{13} \times \sqrt{13}$ 1*T* polymorph show the so-called Star of David, in which all atoms move toward the center of the star. (b) STM topography of annealed 1*T*-TaS_2 obtained at 4.5 K (V_g = −0.4 V, I_t = 400 pA), showing a 3 × 3 periodicity. Scale bar, 5 nm. (c) FFT image of (b). The outmost six spots are due to the 1 × 1 periodicity. The spots due to the 3 × 3 periodicity are marked by arrows, four of which are yellow-colored, indicating the strong spots, and two of which are white-colored, indicating the weak spots. (d) STM topography of annealed 1*T*-TaS_2 obtained at 10 K (V_g = −0.4 V, I_t = 400 pA). Scale bar, 5 nm. (e) FFT image of (d) showing clearly the $\sqrt{13} \times \sqrt{13}$ periodicity.

43 meV/f.u. Including spin−orbit coupling (SOC) in the calculations produced the same results. Since the 2*H* polymorph is more thermodynamically stable than 1*T*, these results explain why annealing bulk 1*T* crystal in a vacuum activates the transition to 2*H*.

The coexistence of superconductivity and CDW provides important clues to the mechanism for enhanced T_c.[48−50] Given the competition between CDW and the superconducting phase, increasing T_c by suppressing CDW is one of the most significant challenges in high-T_c superconductivity research, for which similar strategies have been applied on TMDs.[25,51] The formation of the $\sqrt{13} \times \sqrt{13}$ CCDW in the 1*T* polymorph opens a wide band gap and prohibits superconductivity. In the case of the 2*H* polymorph, while the DOS at the Fermi level is significantly reduced by the formation of the 3 × 3 CDW, it is still finite[14,19,25,52] (Supplementary Figure S3). It has been proposed that in few-layer 2*H* samples the CDW is suppressed, which leads to enhanced T_c. The main evidence of CDW suppression is based on the vanishing of the commonly observed turning point in the *R*−*T* curve at around 77 K as the thickness scales to the 2D limit.[11,25,26] However, in atomically thin 2*H*-TaS_2, the relationship between the 3 × 3 CDW and the superconducting phase is not clear.[25] We did not observe the 3 × 3 CDW on the surface-switched superconducting sample at 77.8 K by STM at first. However, lowering the temperature to 4.5 K causes the 3 × 3 CDW phase to emerge, as shown in Figure 6b, where a weak 3 × 3 superstructure overlapping on a 1 × 1 2*H* surface can be seen. The periodicity of this superstructure can be resolved by a Fourier transform of the STM image, as shown in Figure 6c, where other than the six 1 × 1 spots, extra spots due to a 3 × 3 periodicity, as marked by arrows, can be clearly identified. The direct observation of 3 × 3 CDW down to 4.5 K suggests the possible coexistence of superconductivity and CDW in monolayer 2*H*-TaS_2.

Once the sample temperature is increased to ∼10 K, the 3 × 3 CDW disappears, as shown in Figure 6d, and only the $\sqrt{13} \times \sqrt{13}$ lattice spots, originating from the second layer, can be observed in the Fourier transform in Figure 6e. This result suggests a significantly lower CDW transition temperature than that in bulk 2*H*-TaS_2. The formation of CDWs typically reduces the DOS near E_F. In the 1*T*-phase, the DOS will be reduced to zero; that is, a gap opens, which completely suppresses the superconductivity.[25] In the 2*H* phase, the DOS at E_F is still finite, which is responsible for the observed T_c. Our observation of a partly suppressed 3 × 3 CDW is consistent with the enhanced T_c.

To study the electronic coupling between monolayer 2*H*-TaS_2 on the 1*T*-TaS_2 substrate, a model was built for DFT calculations, in which the substrate is made of two layers of 1*T*-TaS_2, both of which are in the $\sqrt{13} \times \sqrt{13}$ CDW phase with the star centers aligned. A monolayer of 2*H*-TaS_2 with the 1 × 1 lattice structure is allowed to adsorb on top of the bilayer 1*T* substrate, as shown schematically in Figure 7a. Figure 7d and e show the calculated band structure and density of states of the 2*H*-1*T* heterostructure, respectively. Figure 7e shows the DOS projection onto the 2*H* monolayer and the 1*T* substrate, where only the Ta 5d components are shown because they dominate the electronic structure near E_F (set as 0 eV). The calculated DOS is consistent with the STS measurement shown in Figure 2d, revealing a dip near E_F, a sharp increase below E_F with a peak at −0.3 eV, and a small increase above E_F. It can be seen that the Ta 5d DOS states in the 2*H* monolayer (the blue dots in Figure 7d and the blue line in Figure 7e) mainly spread from −0.5 eV to about +1.3 eV. By analyzing the charge densities, we can identify that the d band of the 2*H* monolayer is contributed by the d_{z^2} states. There are clear energy gaps that separate the d_{z^2} band from higher and lower bands. Due to the narrowness of the d_{z^2} band, STM or STS measurement samples the 2*H* monolayer only when the bias is in the region of about

DOI: 10.1021/acsnano.8b07379
ACS Nano 2018, 12, 12619−12628

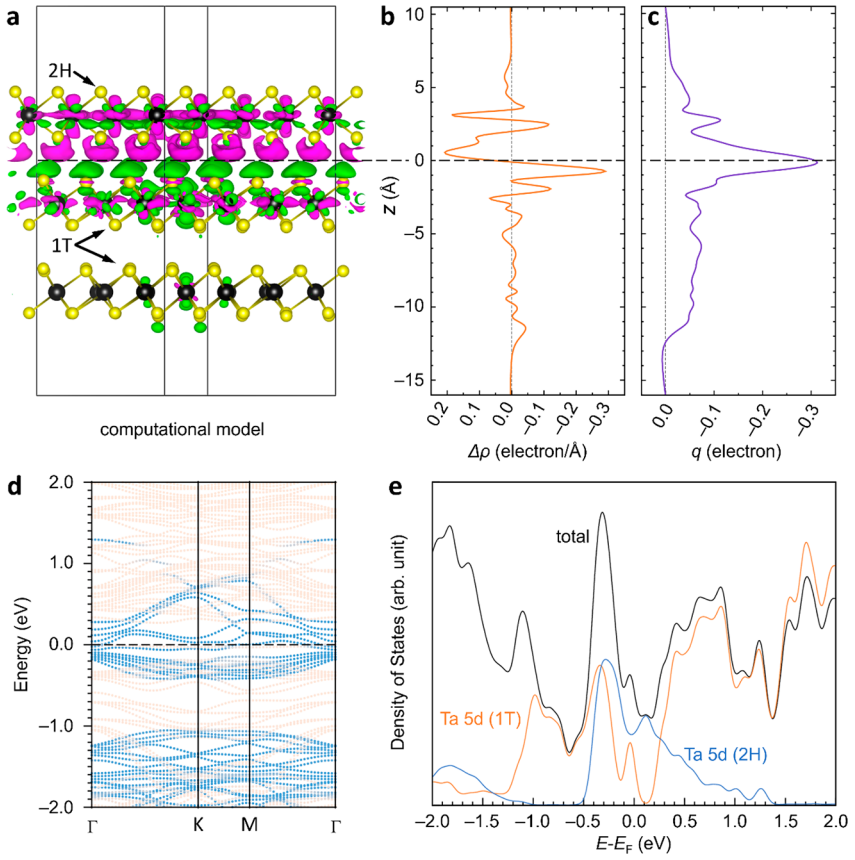

Figure 7. Electronic structure of the 2*H*-1*T* TaS_2 vdW heterostructure and charge transfer doping across the interface. (a) Atomic structure of the model system used to simulate one monolayer of 2*H*-TaS_2 on the bilayer 1*T*-TaS_2 substrate. The structure was relaxed using the SCAN-rVV10 functional. The isosurfaces show the charge density difference, where the green color represents charge deficiency and the purple color represents charge excess. (b) Charge density difference (see text) averaged in the *x*−*y* basal plane. (c) Integrated charge difference from the bottom of the supercell (*i.e.*, at $z = -16$ Å). (d) Band structure and (e) DOS of the model 2*H*-1*T* TaS_2 vdW heterostructure in (a). In the band structure plot, each state is projected onto the 1*T* substrate and the 2*H* monolayer. States with larger projection on the 2*H* monolayer or 1T substrate are plotted in blue or light brown color, respectively. Similarly, the projections of DOS on the Ta 5d states in the 2*H* monolayer and 1*T* substrate are shown by blue and brown lines, respectively. The dashed line in (b), (c), and (d), which extends into (a), marks the center of the vdW gap between the substrate and the 2*H* monolayer, which is taken as the interface.

−0.5 to about +0.5 eV, beyond which the electronic states from the 1*T* substrate will dominate the spectrum. This explains that at high bias (either positive or negative) the topmost 2*H* monolayer TaS_2 becomes "transparent" and STM can see through the top layer and resolve the $\sqrt{13} \times \sqrt{13}$ CDW from the second layer, as shown in Figure 5b and d.[15]

Another possible T_c enhancement mechanism is the charge doping from the substrate,[53,54] which has been proposed to be crucial for a monolayer FeSe high-T_c superconductor.[29,30] Electron doping was also reported to suppress CDW in TMDs.[55] In general, excess charge could influence phase stability in TMDs. For example, electrostatic doping of 2*H* phase $TaSe_2$ can lead to a structural phase transition to the 1*T* phase.[56] Similar transitions can also be induced by STM tips.[45,57] Our DFT calculations of monolayer 1*T*- and 2*H*-TaS_2 show that 1*T*-TaS_2 has a significantly smaller work function (5.35 eV for the $\sqrt{13} \times \sqrt{13}$ CDW phase) than that of 2*H*-TaS_2 (6.07 eV for the 3 × 3 CDW phase). This difference results in electron doping from the 1*T* substrate to the topmost 2*H* monolayer, as shown in Figure 7b and c. To verify the presence of charge transfer, we calculate the difference of the charge densities of the whole system and the separated 1*T* substrate and 2*H* top layer by $\Delta\rho = \rho_{tot} - \rho_{sub} = \rho_{tot} - \rho_{1T-sub} - \rho_{2H-top}$ where ρ_{tot}, ρ_{1T-sub}, and ρ_{2H-top} are plane-averaged (in the *x*−*y* basal plane) charge densities of the whole model, the 1*T* substrate, and the 2*H* top layer, respectively. ρ_{1T-sub} and ρ_{2H-top} were calculated by removing the 2*H* monolayer and the 1*T* substrate, respectively, while maintaining the atomic structures unchanged. As can be seen in Figure 7b, on the 1*T* substrate side (*i.e.*, the part lower than the horizontal dashed line), there is an overall charge density reduction, while in the 2*H* monolayer there is a charge density accumulation. This charge transfer can also be visualized in the plot of charge density difference in Figure 7a, where the green color isosurface represents charge deficiency and the purple color represents charge excess. Figure 7c shows the integrated charge (q) from the bottom of the supercell (*i.e.*, from about $z = -16$ Å). At the interface between the 1*T* substrate and 2*H* top layer (*i.e.*, at $z = 0$ Å), the total charge deficiency from the 1*T* substrate (*i.e.*, the total transferred charge to the 2*H* monolayer) is about 0.31 electron per $\sqrt{13} \times \sqrt{13}$ cell.

CONCLUSION

We have discovered that a 1*T*-to-2*H* polymorph transition can be induced on the surface of bulk 1*T*-TaS_2 (<100 nm thick) simply by thermal annealing. The relaxation is most pronounced at the surface due to larger freedom for atom displacement, which allows the thermodynamically more stable

DOI: 10.1021/acsnano.8b07379
ACS Nano 2018, 12, 12619−12628

2*H* polymorph to manifest. STM measurement confirms that the transition to 2*H*-TaS_2 occurs in the topmost layer only, thus affording a surface-confined 2D superconductivity with a T_c of 2.1 K, which is significantly enhanced from that of the bulk 2*H* crystal. STM measurement further evidences that the 3 × 3 CDW phase is suppressed and exists at 4.5 K in the 2*H* monolayer, which could be correlated to the enhanced T_c. DFT calculation reveals the presence of transfer doping of electrons from the 1*T* substrate to the 2*H* monolayer, which may contribute to the enhanced T_c. Our work provides a simple method to fabricate a CDW Mott-insulator/superconductor vdW heterostructure, which could serve as a platform to study the proximity effect of CDW on superconductivity.

METHODS

STM/STS Measurements. Our experiments were performed in an Omicron UHV system containing a sample preparation chamber (base pressure below 5×10^{-10} mbar) and an analysis chamber (base pressure below 2×10^{-11} mbar) equipped with a low-temperature STM. To avoid surface contamination in the air, a freshly cleaved 1*T*-TaS_2 sample was quickly transferred into the preparation chamber. The sample was annealed at about 200−250 °C for 2−3 h by applying a dc current and then cooled to room temperature before transferring to the analysis chamber to carry out STM experiment. STS measurements were performed in constant-height mode using standard lock-in technique (f = 773.1 Hz, V_{rms} = 16 mV). The dI/dV spectrum taken on a Au(111) surface was used as the reference for tip calibration.

Transport Measurement. For transport measurements, the devices were fabricated by the standard electron beam lithography process using poly(methyl methacrylate) (PMMA) as positive resist. Electrodes were deposited through thermal deposition of Cr (5 nm)/Au (65 nm), as shown in Figure S1. A thin h-BN flake (∼20 nm) was transferred on top of the test samples in a nitrogen-filled glovebox as an encapsulation layer to avoid oxidation in the air during measurements. Low-temperature transport measurements were performed in a 4He cryostat and a 3He/4He dilution cryostat with a standard four-probe setup.

XPS Measurements. High-resolution photoemission spectroscopy (PES) was performed using the beamline facilities in the National Synchrotron Radiation Laboratory (NSRL, China). All the measurements were performed at room temperature in a UHV chamber equipped with a Scienta R4000 electron energy analyzer and with a base pressure of 1×10^{-10} mbar. The S 2p and Ta 4f spectra were measured using 240 eV photon energy with an energy resolution of 24 meV and a beam spot size of 0.2(H) × 0.1(V) mm^2. The photon energy was calibrated using the Au $4f_{7/2}$ core-level peak (84.0 eV) of gold foil in electrical contact with the sample. The least-squares peak fit was performed employing a Shirley background subtraction, asymmetric peak profiles for TaS_2 species, and Voigt photoemission profiles with constant Lorentzian (10%) and Gaussian (90%) line shapes for TaO_x species. For S 2p and Ta 4f doublets, the spin−orbit splitting differences of ∼1.19 eV with a branching ratio of 2 (2 $p_{3/2}$):1 (2 $p_{1/2}$) and ∼1.88 eV with a branching ratio of 8 (4 $f_{7/2}$): 6 (4 $f_{5/2}$) were used for peak fitting, respectively. The full width at half-maximum for each doublet was fixed during the peak-fitting process. The 1T-TaS_2 flake samples were prepared in a glovebox and directly adhered on molybdenum sample holders by gentle pressure; then the sample was transferred quickly to a PES chamber within a few of minutes of air expose. The annealing process was carried out in an adjoined UHV preparation chamber (base pressure $<5 \times 10^{-10}$ mbar).

Raman Measurements. An NT−MDT Raman spectroscopy system with a 633 nm He−Ne wavelength laser was employed to conduct a low-temperature Raman measurement. The laser was focused on the sample through a 50× objective, with a 1 μm spot size. The sample was mounted in a sealed temperature chamber, with a pressure below 1×10^{-2} Torr to minimize oxidation and to ensure effective cooling during the measurement. The measurement temperature can be lowered to 78 K in a cold−hot cell with a temperature stability of ±0.1 K.

DFT Calculation. Our calculations were performed using the Vienna *ab Initio* Simulation Package (VASP) employing a planewave basis set. We used the strongly constrained and appropriately normed (SCAN) exchange−correlation functional amended by the rVV10 functional for the vdW interaction. The ion cores were represented by the projector-augmented wave (PAW) potentials. The kinetic cutoff energy for the planewaves was set to 40 Ry; 18 × 18 × 1, 6 × 6 × 1, and 5 × 5 × 1 k-point grids were used for the (1 × 1), (3 × 3), and ($\sqrt{13} \times \sqrt{13}$) supercells, respectively. Structural optimizations were carried out until the force on each atom was smaller than 0.5 mRy/Bohr. Spin−orbit interaction was added to the all-electron part of the PAW Hamiltonian by a variational treatment in VASP.

ASSOCIATED CONTENT

Supporting Information

The Supporting Information is available free of charge on the ACS Publications website at DOI: 10.1021/acsnano.8b07379.

Sample preparation for 1*T*-TaS_2 flakes; low-temperature Raman characterization for a 1*T*-TaS_2 flake before and after annealing (PDF)

AUTHOR INFORMATION

Corresponding Authors

*E-mail: phyxuh@gmail.com.
*E-mail: chmlohkp@nus.edu.sg.

ORCID

Yi-Yang Sun: 0000-0002-0356-2688
Ibrahim Abdelwahab: 0000-0002-0107-5827
Liang Cao: 0000-0001-7453-7060
Junfa Zhu: 0000-0003-0888-4261
Hai Xu: 0000-0002-4047-7087
Kian Ping Loh: 0000-0002-1491-743X

Author Contributions

#Z. Wang and Y.-Y. Sun contributed equally to this work.

Author Contributions

H.X. and K.P.L. conceived the project. Z.W., I.A., and L.Chu prepared the devices and performed transport. Y.Y.S. performed the DFT calculations. H.X., L.Cao, and Y.W. carried out PES measurement and performed data analysis. H.X. and Z.W. performed STM experiments. H.X., Y.Y.S., Z.W., and K.P.L. wrote the paper. Z.W. and L.Chu performed Raman measurements. W.F. drew the illustration in Figure 2a. All authors contributed to the data analysis and read the manuscript.

Notes

The authors declare no competing financial interest.

ACKNOWLEDGMENTS

K.P.L. acknowledges support from National Research Foundation, Prime Minister's office, Midsized Centre Fund. Y.Y.S. and L.C. acknowledge support from the National Natural Science Foundation of China (Grant Nos. 11774365, 11574317, and 21503233). L.C. acknowledges project support by the State Key Laboratory of Luminescence and Applications (Grant No. SKLA-2018-02). The authors thank beamline BL11U at NSRL for providing the beam time. H.X. thanks the support from the National Natural Science Foundation of China (Grant No. 11774341) and the 100 Talents Program of the Chinese Academy of Sciences.

DOI: 10.1021/acsnano.8b07379
ACS Nano 2018, 12, 12619−12628

REFERENCES

(1) Foner, S.; McNiff, E. J. Upper Critical Fields of Layered Superconducting $NbSe_2$ at Low Temperature. *Phys. Lett. A* **1973**, *45*, 429−430.

(2) Wilson, J. A.; Di Salvo, F. J.; Mahajan, S. Charge-Density Waves and Superlattices in the Metallic Layered Transition Metal Dichalcogenides. *Adv. Phys.* **1975**, *24*, 117−201.

(3) Mak, K. F.; Lee, C.; Hone, J.; Shan, J.; Heinz, T. F. Atomically Thin MoS_2: A New Direct-Gap Semiconductor. *Phys. Rev. Lett.* **2010**, *105*, 136805.

(4) Jones, A. M.; Yu, H.; Ghimire, N. J.; Wu, S.; Aivazian, G.; Ross, J. S.; Zhao, B.; Yan, J.; Mandrus, D. G.; Xiao, D.; Yao, W. Optical Generation of Excitonic Valley Coherence in Monolayer WSe2. *Nat. Nanotechnol.* **2013**, *8*, 634.

(5) Wang, Q. H.; Kalantar-Zadeh, K.; Kis, A.; Coleman, J. N.; Strano, M. S. Electronics and Optoelectronics of Two-Dimensional Transition Metal Dichalcogenides. *Nat. Nanotechnol.* **2012**, *7*, 699.

(6) Li, Y.; Kang, J.; Li, J. Indirect-to-Direct Band Gap Transition of the ZrS_2 Monolayer by Strain: First-Principles Calculations. *RSC Adv.* **2014**, *4*, 7396−7401.

(7) Tsen, A. W.; Hovden, R.; Wang, D.; Kim, Y. D.; Okamoto, J.; Spoth, K. A.; Liu, Y.; Lu, W.; Sun, Y.; Hone, J. C.; Kourkoutis, L. F.; Kim, P.; Pasupathy, A. N. Structure and Control of Charge Density Waves in Two-Dimensional *1T*-TaS_2. *Proc. Natl. Acad. Sci. U. S. A.* **2015**, *112*, 15054−15059.

(8) Ma, L.; Ye, C.; Yu, Y.; Lu, X. F.; Niu, X.; Kim, S.; Feng, D.; Tománek, D.; Son, Y.-W.; Chen, X. H.; Zhang, Y. B. A Metallic Mosaic Phase and the Origin of Mott-Insulating State in *1T*-TaS_2. *Nat. Commun.* **2016**, *7*, 10956.

(9) Chatterjee, U.; Zhao, J.; Iavarone, M.; Di Capua, R.; Castellan, J. P.; Karapetrov, G.; Malliakas, C. D.; Kanatzidis, M. G.; Claus, H.; Ruff, J. P. C.; Weber, F. Emergence of Coherence in the Charge-Density Wave State of *2H*-$NbSe_2$. *Nat. Commun.* **2015**, *6*, 6313.

(10) Xi, X.; Wang, Z.; Zhao, W.; Park, J.-H.; Law, K. T.; Berger, H.; Forró, L.; Shan, J.; Mak, K. F. Ising Pairing in Superconducting $NbSe_2$ Atomic layers. *Nat. Phys.* **2016**, *12*, 139.

(11) de la Barrera, S. C. S.; Sinko, M. R.; Gopalan, D. P.; Sivadas, N.; Seyler, K. L.; Watanabe, K.; Taniguchi, T.; Tsen, A. W.; Xu, X.; Xiao, D. Tuning Ising Superconductivity With Layer and Spin-Orbit Coupling in Two-Dimensional Transition-Metal Dichalcogenides. *Nat. Commun.* **2018**, *9*, 1427.

(12) Sipos, B.; Kusmartseva, A. F.; Akrap, A.; Berger, H.; Forró, L.; Tutiš, E. From Mott State to Superconductivity in *1T*-TaS_2. *Nat. Mater.* **2008**, *7*, 960.

(13) Stojchevska, L.; Vaskivskyi, I.; Mertelj, T.; Kusar, P.; Svetin, D.; Brazovskii, S.; Mihailovic, D. Ultrafast Switching to a Stable Hidden Quantum State in an Electronic Crystal. *Science* **2014**, *344* (6180), 177−180.

(14) Meyer, S. F.; Howard, R. E.; Stewart, G. R.; Acrivos, J. V.; Geballe, T. H. Properties of Intercalated *2H*-$NbSe_2$, 4hb-TaS_2, and *1T*-TaS_2. *J. Chem. Phys.* **1975**, *62*, 4411−4419.

(15) Ekvall, I.; Kim, J.-J.; Olin, H. a. Atomic and Electronic Structures of the Two Different Layers in *4hb*-TaS_2 at 4.2 K. *Phys. Rev. B: Condens. Matter Mater. Phys.* **1997**, *55*, 6758−6761.

(16) Svetin, D.; Vaskivskyi, I.; Brazovskii, S.; Mihailovic, D. Three-Dimensional Resistivity and Switching between Correlated Electronic States in *1T*-TaS_2. *Sci. Rep.* **2017**, *7*, 46048.

(17) Cho, D.; Cheon, S.; Kim, K.-S.; Lee, S.-H.; Cho, Y.-H.; Cheong, S.-W.; Yeom, H. W. Nanoscale Manipulation of the Mott Insulating State Coupled to Charge Order in *1T*-TaS_2. *Nat. Commun.* **2016**, *7*, 10453.

(18) Yu, Y.; Yang, F.; Lu, X. F.; Yan, Y. J.; Cho, Y.-H.; Ma, L.; Niu, X.; Kim, S.; Son, Y.-W.; Feng, D.; Li, S. Gate-Tunable Phase Transitions in Thin Flakes of *1T*-TaS_2. *Nat. Nanotechnol.* **2015**, *10*, 270.

(19) Salvo, F. J. D.; Schwall, R.; Geballe, T. H.; Gamble, F. R.; Osiecki, J. H. Superconductivity in Layered Compounds with Variable Interlayer Spacings. *Phys. Rev. Lett.* **1971**, *27*, 310−313.

(20) Coleman, R. V.; Giambattista, B.; Hansma, P. K.; Johnson, A.; McNairy, W. W.; Slough, C. G. Scanning Tunnelling Microscopy of Charge-Density Waves in Transition Metal Chalcogenides. *Adv. Phys.* **1988**, *37*, 559−644.

(21) Kim, K.; Choi, J.-Y.; Kim, T.; Cho, S.-H.; Chung, H.-J. A Role for Graphene in Silicon-Based Semiconductor Devices. *Nature* **2011**, *479*, 338.

(22) Frindt, R. F. Superconductivity in Ultrathin $NbSe_2$ Layers. *Phys. Rev. Lett.* **1972**, *28*, 299−301.

(23) Wang, H.; Huang, X.; Lin, J.; Cui, J.; Chen, Y.; Zhu, C.; Liu, F.; Zeng, Q.; Zhou, J.; Yu, P.; Wang, X. High-Quality Monolayer Superconductor $NbSe_2$ Grown by Chemical Vapour Deposition. *Nat. Commun.* **2017**, *8*, 394.

(24) Pan, J.; Guo, C.; Song, C.; Lai, X.; Li, H.; Zhao, W.; Zhang, H.; Mu, G.; Bu, K.; Lin, T.; Xie, X. Enhanced Superconductivity in Restacked TaS_2 Nanosheets. *J. Am. Chem. Soc.* **2017**, *139*, 4623−4626.

(25) Yang, Y. F., S; Fatemi, V.; Ruhman, J.; Navarro-Moratalla, E.; Watanabe, K.; Taniguchi, T.; Kaxiras, E.; Jarillo-Herrero, P. Enhanced Superconductivity and Suppression of Charge-Density Wave Order in *2H*-TaS_2 in the Two-Dimensional Limit. *arXiv preprint arXiv:1711.00079* **2017**.

(26) Navarro-Moratalla, E.; Island, J. O.; Manas-Valero, S.; Pinilla-Cienfuegos, E.; Castellanos-Gomez, A.; Quereda, J.; Rubio-Bollinger, G.; Chirolli, L.; Silva-Guillen, J. A.; Agrait, N.; Steele, G. A. Enhanced Superconductivity in Atomically Thin TaS_2. *Nat. Commun.* **2016**, *7*, 11043.

(27) Rui, Z.; Benjamin, G.; Ram Krishna, G.; Stephen, H.; Baoming, W.; Ke, W.; Natalie, B.; Aman, H.; Suman, D.; Joshua, R. Two-Dimensional Tantalum Disulfide: Controlling Structure and Properties *via* Synthesis. *2D Mater.* **2018**, *5*, 025001.

(28) Nakata, Y.; Yoshizawa, T.; Sugawara, K.; Umemoto, Y.; Takahashi, T.; Sato, T. Selective Fabrication of Mott-Insulating and Metallic Monolayer TaSe2. *ACS Appl. Nano Mater.* **2018**, *1*, 1456−1460.

(29) Lee, J. J.; Schmitt, F. T.; Moore, R. G.; Johnston, S.; Cui, Y. T.; Li, W.; Yi, M.; Liu, Z. K.; Hashimoto, M.; Zhang, Y.; Lu, D. H. Interfacial Mode Coupling as the Origin of the Enhancement of Tc in Fese Films on $Srtio_3$. *Nature* **2014**, *515*, 245.

(30) Fan, Q.; Zhang, W. H.; Liu, X.; Yan, Y. J.; Ren, M. Q.; Peng, R.; Xu, H. C.; Xie, B. P.; Hu, J. P.; Zhang, T.; Feng, D. L. Plain S-Wave Superconductivity in Single-Layer Fese on $Srtio_3$ Probed by Scanning Tunnelling microscopy. *Nat. Phys.* **2015**, *11*, 946.

(31) Saito, Y.; Nakamura, Y.; Bahramy, M. S.; Kohama, Y.; Ye, J.; Kasahara, Y.; Nakagawa, Y.; Onga, M.; Tokunaga, M.; Nojima, T.; Yanase, Y. Superconductivity Protected by Spin−Valley Locking in Ion-Gated MoS_2. *Nat. Phys.* **2016**, *12*, 144.

(32) Brouwer, R.; Jellinek, F. The Low-Temperature Superstructures of *1T*-$TaSe_2$ and *2H*-$TaSe_2$. *Physica B+C* **1980**, *99*, 51−55.

(33) Blaha, P. Electronic Structure and Electric Field Gradients in *2H*-TaS_2, $LiTaS_2$ and $SnTaS_2$. *J. Phys.: Condens. Matter* **1991**, *3*, 9381.

(34) Guo, G. Y.; Liang, W. Y. Electronic Structures of Intercalation Complexes of the Layered Compound *2H*-Tas_2. *J. Phys. C: Solid State Phys.* **1987**, *20*, 4315.

(35) Thomson, R. E.; Burk, B.; Zettl, A.; Clarke, J. Scanning Tunneling Microscopy of the Charge-Density-Wave Structure in *1T*-TaS_2. *Phys. Rev. B: Condens. Matter Mater. Phys.* **1994**, *49*, 16899−16916.

(36) Chandrasekhar, B. S. A Note on the Maximum Critical Field of High-Field Superconductors. *Appl. Phys. Lett.* **1962**, *1*, 7−8.

(37) Clogston, A. M. Upper Limit for the Critical Field in Hard Superconductors. *Phys. Rev. Lett.* **1962**, *9*, 266−267.

(38) Haviland, D. B.; Liu, Y.; Goldman, A. M. Onset of Superconductivity in the Two-Dimensional Limit. *Phys. Rev. Lett.* **1989**, *62*, 2180−2183.

(39) Sugai, S.; Murase, K.; Uchida, S.; Tanaka, S. Comparison of the Soft Modes in Tantalum Dichalcogenides. *Physica B+C* **1981**, *105*, 405−409.

DOI: 10.1021/acsnano.8b07379
ACS Nano 2018, 12, 12619−12628

(40) Sugai, S.; Murase, K.; Uchida, S.; Tanaka, S. Studies of Lattice Dynamics in 2*H*-TaS_2 by Raman Scattering. *Solid State Commun.* **1981**, *40*, 399−401.
(41) Sugai, S. Lattice Vibrations in the Charge-Density-Wave States of Layered Transition Metal Dichalcogenides. *Phys. Status Solidi B* **1985**, *129*, 13−39.
(42) Tison, Y.; Martinez, H.; Baraille, I.; Loudet, M.; Gonbeau, D. X-Ray Photoelectron Spectroscopy and Scanning Tunneling Microscopy Investigations of the Solid Solutions $Ti_xTa_{1-X}S_2$ ($0 \leqslant X \leqslant 1$). *Surf. Sci.* **2004**, *563*, 83−98.
(43) Eppinga, R.; Sawatzky, G. A.; Haas, C.; Bruggen, C. F. V. Photoelectron Spectra of 2*H*-TaS_2 and Sn_xTaS_2. *J. Phys. C: Solid State Phys.* **1976**, *9*, 3371.
(44) Hughes, H. P.; Pollak, R. A. Charge Density Waves in Layered Metals Observed by X-Ray Photoemission. *Philos. Mag.* **1976**, *34*, 1025−1046.
(45) Zhang, J.; Liu, J.; Huang, J. L.; Kim, P.; Lieber, C. M. Creation of Nanocrystals through a Solid-Solid Phase Transition Induced by an Stm Tip. *Science* **1996**, *274*, 757−760.
(46) Yoshida, M.; Ye, J.; Zhang, Y.; Imai, Y.; Kimura, S.; Fujiwara, A.; Nishizaki, T.; Kobayashi, N.; Nakano, M.; Iwasa, Y. Extended Polymorphism of Two-Dimensional Material. *Nano Lett.* **2017**, *17*, 5567−5571.
(47) Wilson, J. A. More Concerning Cdw Phasing in 2*H*-$TaSe_2$. *J. Phys. F: Met. Phys.* **1985**, *15*, 591.
(48) Moncton, D. E.; Axe, J. D.; DiSalvo, F. J. Study of Superlattice Formation in 2*H*-$NbSe_2$ and 2*H*-$TaSe_2$ by Neutron Scattering. *Phys. Rev. Lett.* **1975**, *34*, 734−737.
(49) Uchida, S.; Sugai, S. Infrared and Raman Studies on Commensurate Cdw States in Transition Metal Dichalcogenides. *Physica B+C* **1981**, *105*, 393−399.
(50) Lee, C.-H.; Lee, G.-H.; van der Zande, A. M.; Chen, W.; Li, Y.; Han, M.; Cui, X.; Arefe, G.; Nuckolls, C.; Heinz, T. F.; Guo, J. Atomically Thin P-N Junctions with Van Der Waals Heterointerfaces. *Nat. Nanotechnol.* **2014**, *9*, 676−681.
(51) Albertini, O. R.; Zhao, R.; McCann, R. L.; Feng, S.; Terrones, M.; Freericks, J. K.; Robinson, J. A.; Liu, A. Y. Zone-Center Phonons of Bulk, Few-Layer, and Monolayer 1*T*-TaS_2: Detection of Commensurate Charge Density Wave Phase through Raman Scattering. *Phys. Rev. B: Condens. Matter Mater. Phys.* **2016**, *93*, 214109.
(52) Mattheiss, L. F. Band Structures of Transition-Metal-Dichalcogenide Layer Compounds. *Phys. Rew. B* **1973**, *8*, 3719−3740.
(53) Zhang, W.; Li, Z.; Li, F.; Zhang, H.; Peng, J.; Tang, C.; Wang, Q.; He, K.; Chen, X.; Wang, L.; Ma, X. Interface Charge Doping Effects on Superconductivity of Single-Unit-Cell Fese Films on $Srtio_3$ Substrates. *Phys. Rev. B: Condens. Matter Mater. Phys.* **2014**, *89*, 060506.
(54) Bang, J.; Li, Z.; Sun, Y. Y.; Samanta, A.; Zhang, Y. Y.; Zhang, W.; Wang, L.; Chen, X.; Ma, X.; Xue, Q. K.; Zhang, S. B. Atomic and Electronic Structures of Single-Layer Fese on $SrTiO_3$(001): The Role of Oxygen Deficiency. *Phys. Rev. B: Condens. Matter Mater. Phys.* **2013**, *87*, 220503.
(55) Qian, D.; Hsieh, D.; Wray, L.; Morosan, E.; Wang, N. L.; Xia, Y.; Cava, R. J.; Hasan, M. Z. Emergence of Fermi Pockets in a New Excitonic Charge-Density-Wave Melted Superconductor. *Phys. Rev. Lett.* **2007**, *98*, 117007.
(56) Li, Y.; Duerloo, K.-A. N.; Wauson, K.; Reed, E. J. Structural Semiconductor-to-Semimetal Phase Transition in Two-Dimensional Materials Induced by Electrostatic Gating. *Nat. Commun.* **2016**, *7*, 10671.
(57) Kim, J.-J.; Park, C.; Yamaguchi, W.; Shiino, O.; Kitazawa, K.; Hasegawa, T. Observation of a Phase Transition from the T Phase to the H Phase Induced by a Stm Tip in 1*T*-TaS_2. *Phys. Rev. B: Condens. Matter Mater. Phys.* **1997**, *56*, R15573−R15576.

DOI: 10.1021/acsnano.8b07379
ACS Nano 2018, 12, 12619−12628